Robust Design for the Roll-Channel Autopilot of a Canard-Guided Dual-Spin Projectile

Sovanna Thai, Spilios Theodoulis, Clément Roos, Jean-Marc Biannic

Robust Design for the Roll-Channel Autopilot of a Canard-Guided Dual-Spin Projectile

Sovanna Thai * **Spilios Theodoulis** * **Clément Roos** ** **Jean-Marc Biannic** **

* *Department of Guidance, Navigation and Control, French-German Research Institute of Saint-Louis, 5 rue du Général Cassagnou, 68301, Saint-Louis, FR*
** *Information Processing and Systems Department, ONERA The French Aerospacelab, 2 avenue Edouard Belin, 31400, Toulouse, FR*

Abstract: This article addresses the design of a robust feedback controller for the roll dynamics of a dual-spin guided projectile equipped with low performance actuators. Exploiting characteristics of realistic flight scenarios and the corresponding parameter variations, a simple yet efficient gain-scheduling strategy tailored for this application is devised. Controller synthesis is based on robust control techniques, and takes into account potential hardware limitations to safeguard against performance loss upon digital implementation. Robust stability analysis with respect to aerodynamic and actuator uncertainties is also investigated using μ-analysis techniques and includes computation of worst-case stability margins. The designed autopilot is then tested on a complete nonlinear simulator of the projectile to validate the proposed solution.

Keywords: Flight dynamics, LPV systems, Robust control, Gain-scheduling, Autopilot design, Guided projectiles

1. INTRODUCTION

The lack of accuracy of standard ballistic projectiles negatively impacts operations in several ways, for instance by increasing the risk of collateral damage and the number of rounds required to intercept a target. Guided projectile concepts integrate steering mechanisms which aim to address these issues (see e.g. Costello (2001); Fresconi (2011)). Among them, the concept of a course correction fuse (CCF) decoupled from the body and equipped with canards is particularly attractive, as it can then be used to retrofit older projectiles. This economic solution leads to a dual-spin guided projectile concept (see Fig. 1), whose precision and performance are then highly dependent on the embedded hardware and flight control algorithms, which must take into account important parameter variations across the trajectory and aerodynamic uncertainties.

The flight scenario of such a projectile can be broken into several phases. In the first one, electronic components are switched on. This is done after launch to avoid possible hardware degradations due to the harsh initial conditions. Then the roll rate of the nose, which at this point is high due to the mechanical bearing between the body and the nose, is decreased in a braking phase. Once the roll rate is sufficiently reduced, the roll autopilot stabilises the roll angle itself, providing the required environment to tackle lateral control for the remaining flight time.

This article addresses the design of a robust feedback controller for the roll dynamics. The proposed nose concept differs from Theodoulis et al. (2013) and Sève et al. (2017), in which the nose roll is controlled with an embedded coaxial motor. Instead, the nose roll is now controlled directly by the canards. This is an improvement in terms of hardware complexity. Exploiting characteristics of realistic flight scenarios, a simple yet efficient gain-scheduling strategy tailored for this application is devised, which requires only a single controller design point. Furthermore, potential hardware limitations are accounted for to avoid overestimation of stability margins. Controller synthesis is based on robust $\mathcal{H}_\infty$ control techniques, while robustness towards parametric uncertainties is tackled using μ-analysis and a thorough modelling of the uncertainties.

The paper is organised as follows: Section 2 gives the full nonlinear model of the nose roll-channel dynamics and the associated LPV model, Section 3 discusses the design of a gain-scheduled autopilot obtained through a unique synthesis performed on a scaled model, Section 4 is dedicated to the robustness analysis of the obtained closed-loop system, and Section 5 shows simulation results on a complete 7DoF nonlinear simulator, validating the proposed solution.

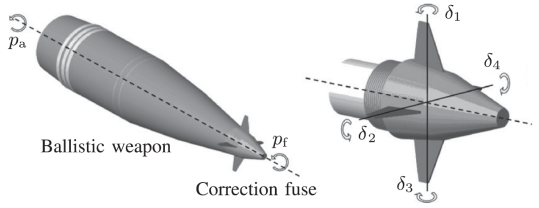

Fig. 1. Dual-spin guided projectile concept with the four canards

2. ROLL DYNAMICS MODELLING

2.1 LPV Modelling

The nonlinear dynamics of the roll angle ϕ_f and roll angular rate p_f of the projectile nose are given by

$$\begin{bmatrix}\dot{\phi}_f \\ \dot{p}_f\end{bmatrix} = \begin{bmatrix} p_f + r\tan\theta \\ I_{xf}^{-1}(L_{f_c} + L_{f-a})\end{bmatrix} \tag{1}$$

with r the body yaw rate and θ the pitch angle, I_{xf} the nose moment of inertia, and L_{f_c} and L_{f-a} the control moments induced by the canards and the front-aft (nose-body) friction respectively. These moments can be modelled as

$$L_{f_c} = \overline{q}SdC_{l\delta}(\mathcal{M})\delta_p \tag{2}$$

$$L_{f-a} = \overline{q}SdC_X(\mathcal{M},\alpha')\,\mathrm{sign}(p_a - p_f)(K_s + K_v|p_a - p_f|) \tag{3}$$

where the aerodynamic coefficient $C_{l\delta}(\mathcal{M})$ is defined as

$$C_{l\delta}(\mathcal{M}) = n \cdot C_{l\delta_i}(\mathcal{M}) \tag{4}$$

with $C_{l\delta_i}(\mathcal{M})$ the deflection moment associated to one canard, and n the number of canards used for roll control. The command signal δ_p is then a virtual signal which is converted into commands $\delta_i, i = 1,\dots,4$ for each of the four canard actuators. If all four canards are used, then the following relation holds (see Siouris (2004)):

$$\delta_p = \frac{\delta_1 + \delta_2 + \delta_3 + \delta_4}{4} \tag{5}$$

Note that this relation is dependent on the choice of sign conventions of the rotations. Alternatively, one may use only one pair (i,j) of canards, in which case

$$\delta_p = \frac{\delta_i + \delta_j}{2} \tag{6}$$

Additional variables appearing in Eqs. (2)-(3) are the drag aerodynamic coefficient $C_X(\mathcal{M},\alpha')$, the body roll rate p_a, and the dynamic pressure $\overline{q} = \frac{1}{2}\rho(h)V^2$, with $\rho(h)$ the altitude-dependent air density, and V the airspeed. The aerodynamic coefficients depend nonlinearly on the Mach number $\mathcal{M} = V/a(h)$, with a the altitude-dependent speed of sound, and the total angle of incidence α'. The constants are the static and viscous friction coefficients K_s and K_v, the projectile calibre d, and the reference surface S.

The roll dynamics can be rewritten in the following linear parameter-varying (LPV) form:

$$\begin{bmatrix}\dot{\phi}_f \\ \dot{p}_f\end{bmatrix} = \begin{bmatrix}0 & 1 \\ 0 & a_{22}(\boldsymbol{\sigma})\end{bmatrix}\begin{bmatrix}\phi_f \\ p_f\end{bmatrix} + \begin{bmatrix}0 \\ b_2(\boldsymbol{\sigma})\end{bmatrix}\delta_p + \begin{bmatrix}d_\phi \\ d_p\end{bmatrix} \tag{7}$$

where

$$\begin{aligned} a_{22}(\boldsymbol{\sigma}) &= -\left(\frac{\overline{q}Sd}{I_{xf}}\right)C_X(\mathcal{M},\alpha')K_v \\ b_2(\boldsymbol{\sigma}) &= -\left(\frac{\overline{q}Sd}{I_{xf}}\right)C_{l\delta}(\mathcal{M}) \end{aligned} \tag{8}$$

and $\boldsymbol{\sigma} = \begin{bmatrix}\alpha' & V & h\end{bmatrix}^T \in \Gamma \subset \mathbb{R}^3$ is a time-varying parameter vector. The time-varying disturbances d_ϕ and d_p are given by

$$\begin{aligned} d_\phi &= r\tan\theta \\ d_p &= \left(\frac{\overline{q}Sd}{I_{xf}}\right)C_X(\mathcal{M},\alpha')[\mathrm{sign}(p_a - p_f)K_s + K_v p_a] \end{aligned} \tag{9}$$

The flight envelope is determined based on ballistic trajectory simulations using standard initial conditions. The results show that in practical flight conditions, $\alpha' \in [0\text{ deg}, 15\text{ deg}]$, thus the drag coefficient, given in Fig. 2, is mostly dependent on Mach number. This observation leads to consider a reduced parameter vector $\boldsymbol{\lambda} = [V\ h]^T$, corresponding to the flight envelope 140 m/s $\leq V \leq$ 400 m/s and 0 m $\leq h \leq$ 15000 m. Fig. 3 shows the variation of the state-space coefficients a_{22} and b_2 over this reduced flight envelope (calculated with $\alpha' = 0$).

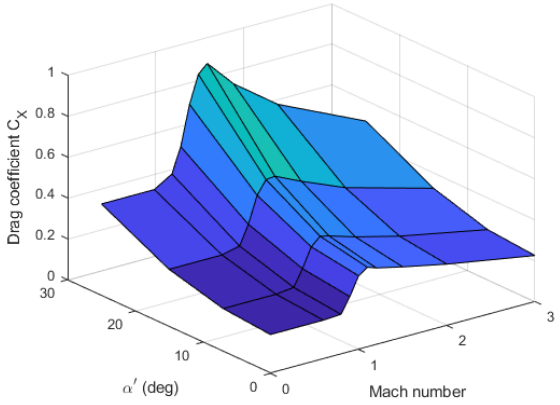

Fig. 2. Drag coefficient $C_X(\mathcal{M},\alpha')$

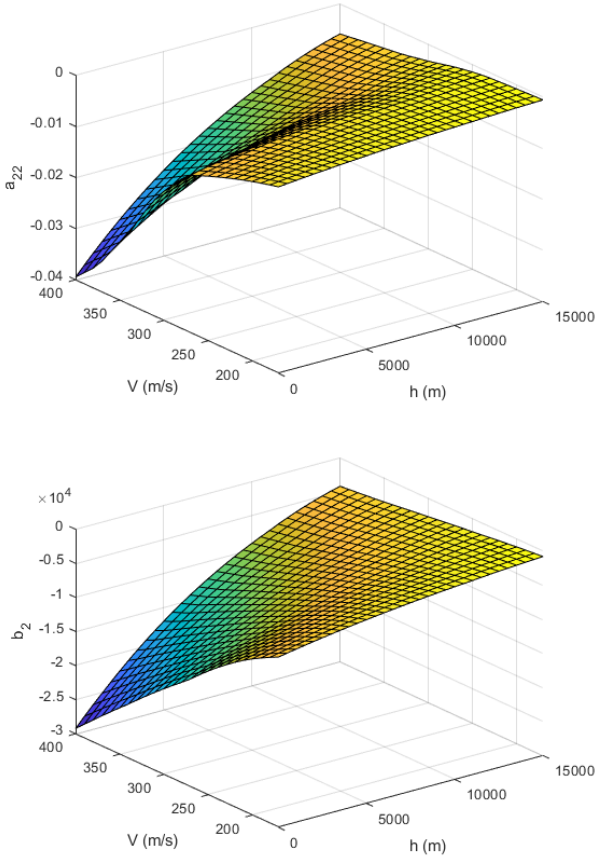

Fig. 3. Variation of the state-space coefficients over the flight envelope

2.2 Complete Open-Loop Model

In addition to the airframe, the open-loop model also includes actuator and sensor dynamics. The actuators are modelled as a second-order system with a natural frequency $\omega_\delta = 20$ Hz and damping ratio $\zeta_\delta = 0.781$, with input and output the commanded and real deflection angles, respectively $\delta_{p,c}$ and δ_p. The selected natural frequency is relatively small compared to the typical natural frequency of actuators embedded in highly manoeuvrable missiles, which is around 40 Hz (see e.g. Tsourdos and White (2005)). For simplicity, sensors are assumed to directly yield measurements $y_m = [\phi_{f,m}\ p_{f,m}]^T$ of ϕ_f and p_f, and are modelled by fast first-order systems with natural frequency $\omega_m = 133$ Hz.

The obtained open-loop model represents the nominal system to be controlled. We further consider ω_δ, ζ_δ, $\overline{q}$, C_X, $C_{l\delta}$, and K_v to be real parametric uncertainties. A 5% uncertainty level is considered on the actuator characteristics ω_δ and ζ_δ. For the dynamic pressure and aerodynamic coefficients, upper and lower bounds are obtained by introducing a 5% uncertainty on mean sea level base temperature $T_0 = 288.15$ K and pressure $P_0 = 101.325$ kPa, which can then be propagated to obtain bounds on the air density and speed of sound as a function of the altitude

$$\rho(h) = \frac{P}{RT} \qquad a(h) = \sqrt{\kappa} RT \tag{10}$$

with κ the adiabatic index, R the specific gas constant, and T and P the temperature and pressure, obtained using the ISA1975 standard atmospheric model (ISO2533c (1997)). Finally, a 40% uncertainty on K_v is considered.

3. ROLL AUTOPILOT DESIGN

3.1 Gain Scheduling Strategy

A typical method to obtain a gain-scheduling controller is to grid the flight envelope, and to compute a controller at each operating point (Rugh and Shamma (2000)). Here we propose a method tailored for the studied system which presents the advantage of requiring a unique and straightforward controller synthesis to cover the whole flight envelope. Indeed, a noticeable property is that the variations of a_{22} are restricted to a small interval. It is therefore tempting to approximate this coefficient with a constant $\overline{a_{22}}$. From Eq. (7), the transfer function of the nose dynamics, i.e. between δ_p and $y = [\phi_f\ p_f]^T$, then takes the form

$$G(s) = b_2(\boldsymbol{\lambda}) \begin{bmatrix} \dfrac{1}{s(s - \overline{a_{22}})} \\ \dfrac{1}{s - \overline{a_{22}}} \end{bmatrix} = b_2(\boldsymbol{\lambda}) \hat{G}(s) \tag{11}$$

Thus, if one designs a controller $\hat{K}(s)$ associated to the LTI system $\hat{G}(s)$, then a gain-scheduled controller for $G(s)$ is directly obtained as

$$K(s) = \frac{1}{b_2(\boldsymbol{\lambda})} \hat{K}(s) \tag{12}$$

hence only one controller design point is needed.

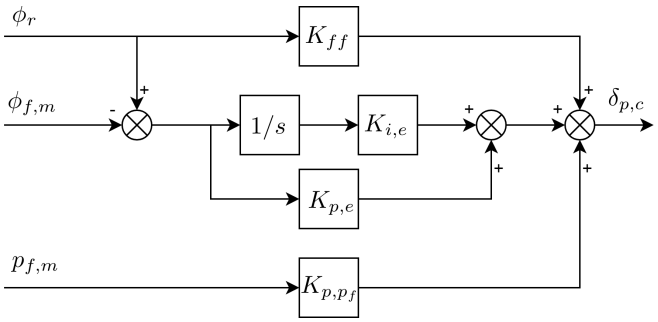

Fig. 4. Autopilot structure for roll angle control

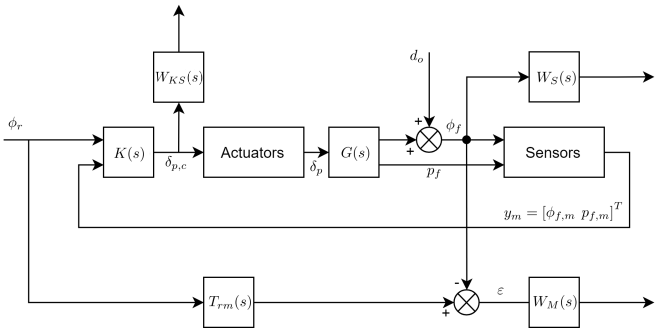

Fig. 5. Closed-loop system

3.2 Autopilot Architecture and Design Approach

The proposed fixed-structure controller is shown in Fig. 4, and consists of a PI-P controller (gains $K_{i,e}, K_{p,e}$, and K_{p,p_f}) with an additional feedforward gain K_{ff} to help with reference signal tracking. To deal with disturbance rejection, a mixed-sensitivity S/KS approach (see e.g. Skogestad and Postlethwaite (2005)) is used to attenuate low frequency disturbances at the plant output and high frequency actuator usage. For simplicity, the disturbance model given by Eq. (9) is not exploited, and a pure additive perturbation d_o on ϕ_f is considered instead. Another requirement is that the transfer from the reference roll angle ϕ_r to the nose roll angle ϕ_f remains as close as possible to a second-order model:

$$T_{rm}(s) = \frac{\omega_{rm}^2}{s^2 + 2\zeta_{rm}\omega_{rm}s + \omega_{rm}^2} \tag{13}$$

A value of $\zeta_{rm} = 0.781$ is taken, which corresponds to an overshoot of 2%, thus minimising the settling time for a given natural frequency ω_{rm}. To further enforce robustness, minimum stability margins $GM > 6$ dB and $PM > 35$ deg are specified at the autopilot output. Thus, and with reference to Fig. 5, the optimisation problem to solve is:

$$\begin{aligned} \underset{\boldsymbol{K}}{\text{minimise}} \quad & \|W_M(s) T_{\phi_r \to \varepsilon}(s, \boldsymbol{K})\|_\infty \\ \text{subject to} \quad & \left\|W_S(s) T_{d_o \to \phi_f}(s, \boldsymbol{K})\right\|_\infty < 1 \\ & \left\|W_{KS}(s) T_{d_o \to \delta_{p,c}}(s, \boldsymbol{K})\right\|_\infty < 1 \\ & GM > 6 \text{ dB}, \quad PM > 35 \text{ deg} \end{aligned} \tag{14}$$

with $\boldsymbol{K} = \begin{bmatrix} K_{i,e} & K_{p,e} & K_{p,p_f} & K_{ff} \end{bmatrix}^T$ and $T_{u \to y}$ denotes the transfer function from input signal u to output signal y. The $W_i(s)$ are weighting filters chosen in accordance with the expected frequency behaviour of the closed-loop system.

From the start, it is known that the controller is to be implemented digitally. Because of the low life-expectancies of the guided projectile once launched, the use of expensive hardware is undesirable. In particular, this restricts the sampling frequency of the autopilot command. If left ignored, this aspect of the implementation could lead to important performance loss between the tuned synthesis model and the digitised model. This issue can be addressed by taking into account the samplers and zero-order-holds of the digital system in the continuous-time synthesis, so that they are adequately compensated from the start. Stevens and Lewis (2003) proposes a way to do so without having to leave the continuous-time framework. The idea is to approximate the transfer function of a sampler plus zero-order-hold of sampling period T

$$G_{0s}(s) = \frac{1 - e^{-sT}}{sT} \tag{15}$$

using Padé approximants of e^{-sT}. A second order approximation $\tilde{G}_{0s}(s)$ of $G_{0s}(s)$ is given by

$$\tilde{G}_{0s}(s) = \frac{1 - sT/10 + (sT)^2/60}{1 + 2sT/5 + (sT)^2/20} \tag{16}$$

Two such transfers are added in the synthesis model. The first, placed between the controller and the actuator, corresponds to the period $T_K = 1/100$ s of emission of the command signal. The second corresponds to the digital treatment done by the separate navigation unit, of period $T_{Nav} = 1/600$ s.

3.3 Tuning Results

The optimisation problem (14) is solved with the MATLAB command `systune`, which uses nonsmooth optimisation algorithms (Apkarian and Noll (2006)). The trade-offs between the different goals are handled by adjusting the weighting filters. These are set as follows:

$$W_M(s) = \frac{s/0.15 + 200}{s + 200 \cdot 10^{-4}} \qquad W_S(s) = \frac{s/1.6 + 4}{s + 4 \cdot 10^{-4}} \tag{17}$$
$$W_{KS}(s) = W_{KS} = 1/400$$

The filter $W_{KS}(s)$ is taken as a constant as good command signal roll-off at high frequency is observed without further adjustments. Note that the unusually large value of $1/W_{KS}$ is due to the scaling coefficient $b_2(\boldsymbol{\lambda})$ between the synthesis model and the LPV model. The frequency ω_{rm} of the reference model $T_{rm}(s)$ is adjusted to achieve the shortest possible settling time. Figs. 6 and 7 show respectively the shaped closed-loop transfers and step response with the synthesised controller, which meets the specified tuning goals and features a satisfying step response with a settling time $t_s = 0.3$ s. Good stability margins are also obtained at the output of the autopilot, with $GM = 3.0 = 9.5$ dB, $PM = 38.1$ deg, and $DM = 28$ ms (more than two autopilot sample periods), with gain crossover frequency $\omega_c = 23.6$ rad/s.

The gain-scheduled controller $K(s) = \frac{1}{b_2(\boldsymbol{\lambda})}\hat{K}(s)$ is then tested on both the continuous model with approximated samplers, and on the digital design, for values of $\boldsymbol{\lambda}$ corresponding to a 24×31 grid of the flight envelope. The results are nearly identical for both models, and it is further verified that the computed gain and delay margins at autopilot output remain relevant on the digitised model, validating

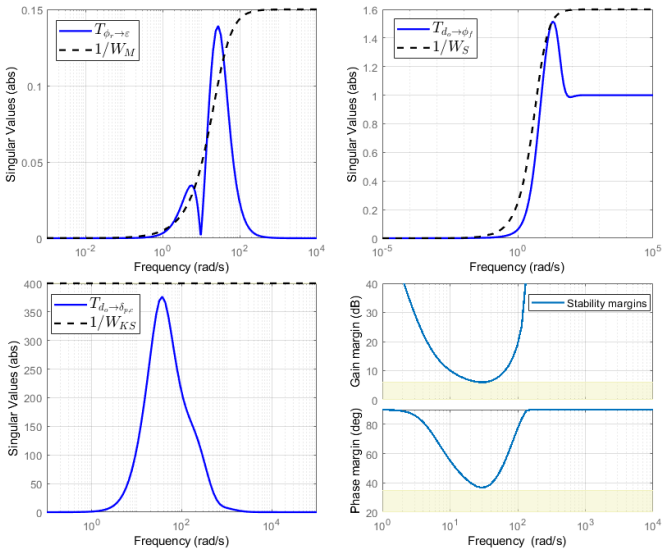

Fig. 6. Shaped closed-loop transfer functions and stability margins

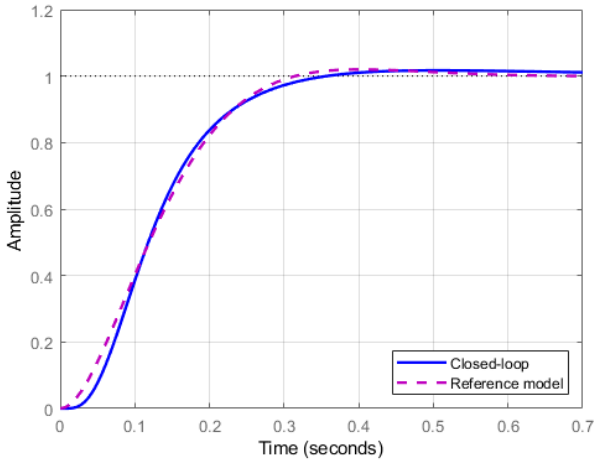

Fig. 7. Closed-loop system step response

the relevance of the approximations made. Fig. 8 shows simulation results on the digital model across the flight envelope, with a scenario featuring a reference signal $\phi_r = 90$ deg and a disturbance $d_o = 20$ deg on ϕ_f at $t = 1.5$ s. As expected, the only noticeable difference between different operating points lies in the amplitude of the deflection angles owing to the important variations of $b_2(\boldsymbol{\lambda})$ over the flight envelope, while differences due to variations of $a_{22}(\boldsymbol{\lambda})$ are indiscernible.

4. ROBUSTNESS ANALYSIS

Robustness against the parametric uncertainties discussed in Section 2 is studied using μ-analysis (Doyle (1982)), whose principles are now briefly reminded. Consider the interconnection depicted in Fig. 9, where $M(s)$ is a stable real-valued LTI plant representing the nominal closed-loop system, and Δ is a block-diagonal LTI operator gathering all real parametric uncertainties

$$\Delta = \text{diag}(\delta_1 I_{n_1}, \ldots, \delta_N I_{nN}) \tag{18}$$

It is assumed that $|\delta_i| \leq 1$ for every $i = 1, \ldots, N$, i.e. the uncertainties are normalised with respect to their bounds.

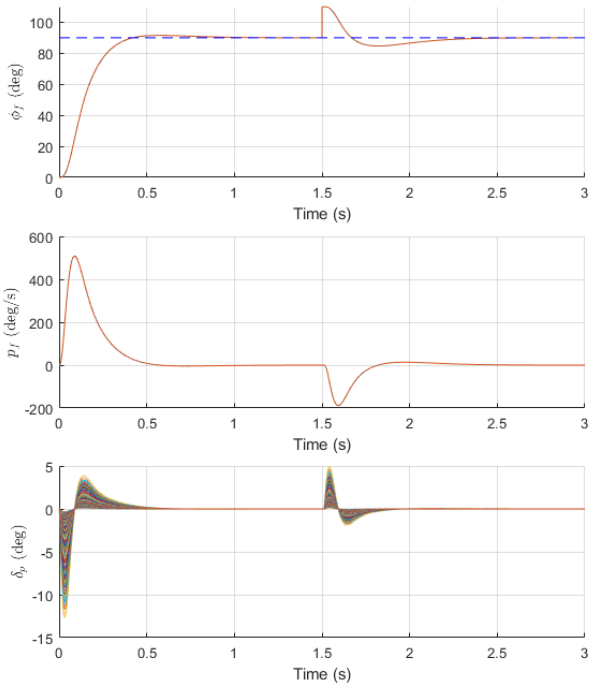

Fig. 8. Digital closed-loop: roll angle, roll rate, and commanded deflection angle

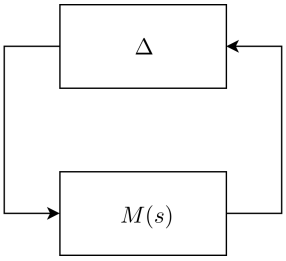

Fig. 9. Interconnection for robust stability analysis

Then the interconnection is stable for all possible values of Δ if and only if

$$\sup_{\omega \in \mathbb{R}_+} \mu_{\mathbf{\Delta}}(M(j\omega)) \leq 1 \tag{19}$$

where $\mu_{\mathbf{\Delta}}(M(j\omega))$ is the structured singular value (SSV). Computing the exact value of μ being NP-hard, upper and lower bounds are usually determined instead. A μ-upper bound provides a guaranteed but conservative robust stability margin, while a μ-lower bound gives the size of a destabilising uncertainty configuration.

For the studied system, the uncertainty block Δ is found to be of the form

$$\Delta = \text{diag}(\delta_{C_X} I_1, \delta_{C_{l\delta}} I_1, \delta_{K_v} I_1, \delta_{\bar{q}} I_1, \delta_{\zeta_\delta} I_1, \delta_{\omega_\delta} I_2) \tag{20}$$

As seen in the previous section, the closed-loop system behaviour varies little over the flight envelope except for the coefficient $b_2(\boldsymbol{\lambda})$ on the command signal $\delta_{p,c}$. However, bounds on the uncertain parameters vary more significantly, hence motivating computation of robust stability margins over the whole flight envelope. Fig. 10 shows the upper bounds on the SSV over a 24×31 grid, obtained using the SMART library of the SMAC Toolbox (Roos (2013)). The values remain significantly less than 1 at every point, indicating good robust stability of the closed-loop system over the whole flight envelope. By adding a fictitious uncertainty δ_M between the autopilot and the plant (Lescher and Roos (2011)), tight upper and lower bounds on the input-output margins at autopilot output are also computed. Fig. 11 shows lower bounds on the worst-case delay margins DM_{wc} on the same grid as before. The surfaces computed for worst-case gain and phase margins are very similar in appearance, with a noticeable drop in the guaranteed margins for high altitudes ($h > 11500$ m). Overall, the lowest guaranteed margins found over the flight envelope are $GM_{wc} \geq 1.70$ (4.6 dB), $PM_{wc} \geq 28.6$ deg, $DM_{wc} \geq 0.014$ s. This means for instance that for some flight points, we can find an uncertainty configuration for which a delay no larger than two sampling periods may cause instability. This can motivate the implementation of a fault-tolerant hardware architecture, or the use of higher performance components.

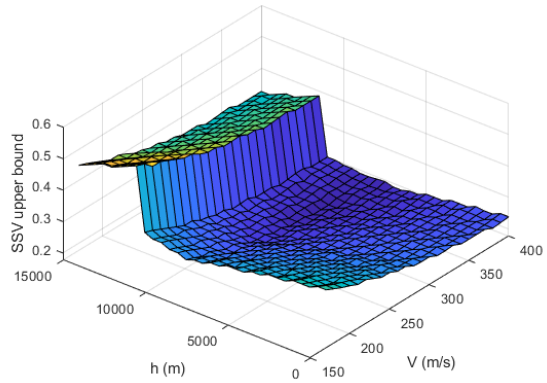

Fig. 10. Upper bound on the SSV over the flight envelope

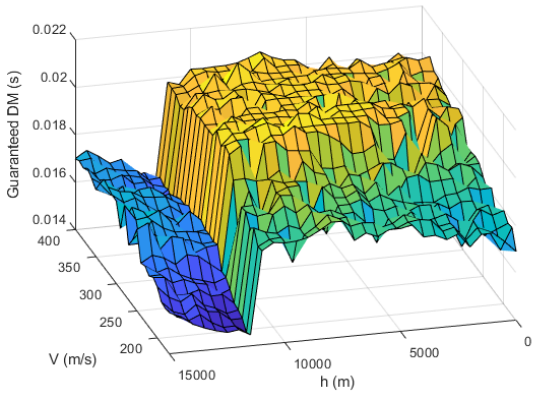

Fig. 11. Guaranteed delay margins with parametric uncertainties over the flight envelope

5. SIMULATION RESULTS

The roll autopilot is now tested on a complete 7DoF nonlinear simulator. The nose braking phase is activated at $t = 20$ s, and roll rate reduction is achieved simply by sending a constant command signal $\delta_p = 10$ deg to the actuators (thus no rate loop is needed). Switching to the designed control law is done when the roll angular rate p_f reduces to 1800 deg/s (5 turns per second). The results are shown in Fig. 12, where the reference

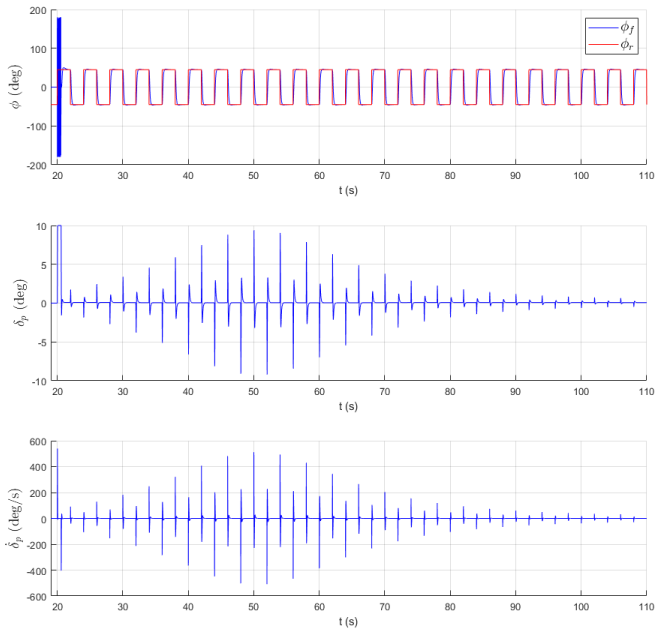

Fig. 12. Roll angle, deflection angle, and deflection rate on the nominal nonlinear simulator

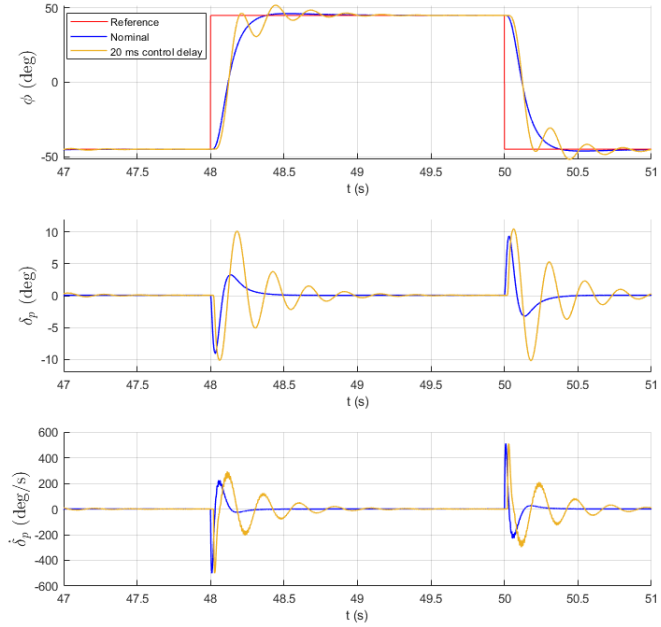

Fig. 13. Roll angle, deflection angle, and deflection rate without/with delay on the command signal

roll angle periodically switches between +45 deg and −45 deg. System performance is satisfying over all the trajectory. The impact of the variation of the scheduling parameters on the amplitude of the control signals is clearly visible, with higher deflection angles occurring when the projectile has high altitude and low velocity, corresponding to higher values of $b_2(\boldsymbol{\lambda})$. These remain well within the effective range of operation of the canards, thus the issue of saturation does not arise. In accordance with the study performed on the linear model, the system remains stable if a delay of 20 ms is added at the output of the autopilot, as illustrated by Fig. 13. The system becomes unstable for a delay of 30 ms, as well as for a gain of 3.1, which are very close values to the nominal margins computed on the linear model in Section 3.3.

6. CONCLUSION

In this article, the problem of controlling the roll channel of a canard-guided spin-stabilised 155mm projectile was tackled. The study of the variations of the system parameters over the flight envelope led to consider a very simple design approach requiring only one controller synthesis on a scaled model. Robustness towards both digital aspects and parametric uncertainties were addressed, the former by enriching the system model used for synthesis, and the latter using μ-analysis techniques along with a detailed description of the uncertainties. The proposed autopilot was then tested on a nonlinear simulator, leading to satisfying results. Future work will focus on the control of the pitch-yaw channel, whose dynamics can be modelled as a quasi-LPV system.

REFERENCES

Apkarian, P., Noll, D., 2006. Nonsmooth H_∞ synthesis. IEEE Transactions on Automatic Control.

Costello, M., 2001. Extended range of a gun launched smart projectile using controllable canards. Shock and Vibration 8.

Doyle, J., 1982. Analysis of feedback systems with structured uncertainties. IEE Proceedings D - Control Theory and Applications 129 (6), 242–250.

Fresconi, F., 2011. Guidance and control of a projectile with reduced sensor and actuator requirements. Journal of Guidance, Control, and Dynamics 34, 1757–1766.

ISO2533c, 1997. International Standard Atmosphere. International Organization for Standardization, Geneva, Switzerland, addendum 2 Edition.

Lescher, F., Roos, C., 2011. Robust stability of time-delay systems with structured uncertainties: a μ-analysis based algorithm. In: Proceedings of the 50th IEEE Conference on Decision and Control. Orlando, Florida, pp. 4955–4960.

Roos, C., 2013. Systems modeling, analysis and control (SMAC) toolbox: An insight into the robustness analysis library. In: Proceedings of the IEEE Conference on Computer Aided Control System Design. pp. 176–181.

Rugh, W. J., Shamma, J. S., 2000. Research on gain scheduling. Automatica.

Siouris, G. M., 2004. Missile Guidance and Control Systems. Springer.

Skogestad, S., Postlethwaite, I., 2005. Multivariable Feedback Control: Analysis and Design, 2nd Edition. Wiley.

Stevens, B. L., Lewis, F. L., 2003. Aircraft Control and Simulation. Wiley.

Sève, F., Theodoulis, S., Wernert, P., Zasadzinski, M., Boutayeb, M., 2017. Gain-scheduled $\mathcal{H}_\infty$ loop-shaping autopilot design for spin-stabilized canard-guided projectiles. AerospaceLab Journal (13), 1–24.

Theodoulis, S., Gassmann, V., Brunner, T., Wernert, P., 2013. Fixed structure robust control design for the 155mm canard-guided projectile roll-channel autopilot. In: Proceedings of the 21st Mediterranean Conference on Control and Automation. pp. 155–160.

Tsourdos, A., White, B. A., 2005. Adaptive flight control design for nonlinear missile. Control Engineering Practice 13 (3), 373 – 382.